Inverse Radiation Problem with Infrared Images to Monitor Plasma-Facing Components Temperature in Metallic Fusion Devices

Charly Talatizi, Marie-Hélène Aumeunier, Fabrice Rigollet, Mickael Le Bohec, Jonathan Gérardin, Jonathan Gaspar, Christophe Le Niliot, Albrecht Herrmann

Inverse Radiation Problem with Infrared Images to Monitor Plasma-Facing Components Temperature in Metallic Fusion Devices

Charly Talatizi[a*], Marie-Hélène Aumeunier[a], Fabrice Rigollet[b], Mickael Le Bohec[b], Jonathan Gérardin[b], Jonathan Gaspar[b], Christophe Le Niliot[b], Albrecht Herrmann[c]

[a]*CEA Cadarache/Institut de Recherche sur la Fusion par confinement Magnétique, 13108 Saint-Paul-lez-Durance cedex, France*
[b]*Aix Marseille Univ., CNRS, IUSTI UMR 7343, Marseille, France*
[c]*Max-Planck-Institut für Plasmaphysik, EURATOM Association, Boltzmannstr. 2, D-85748 Garching, Germany*
[*]*Corresponding author: marie-helene.aumeunier@cea.fr*

Infrared (IR) diagnostics are used to measure plasma-facing components (PFC) surface temperature in fusion devices. However, the interpretation of such images is complex in all-reflective environments because of unknown emissivity and multiple reflections issues. In order to assess these challenges an iterative inversion method based on a fast photonic model, the radiosity method, has been developed. The radiosity method is based on strong hypotheses including all diffuse surfaces. The inversion method allows retrieving the true surface temperature of PFC in two steps: a step of the target emissivity estimation in a baking scene and the use of the emissivity map to retrieve the temperature of metallic components with errors up to 3% during a plasma scenario.

Keywords: infrared thermography, emissivity, reflections, Ray Tracing Monte Carlo, Radiosity method, inverse problem

1. Introduction

Infrared (IR) cameras are key diagnostics to monitor and control Plasma-Facing Components (PFC) in a fusion device. Nevertheless, the use of all-metallic PFC with low and variable emissivity ($\varepsilon \sim 0.1\text{-}0.3$) makes difficult the surface temperature measurement [1]. Indeed, the radiance collected by the IR camera includes both the thermal radiation emitted by the target and a parasitic radiation coming from the surroundings of the target. Furthermore, target emissivity changes with the surface temperature and roughness. This causes major errors on the surface temperature measurement that we need to address in order to achieve high power and safe plasma operation.

An inverse method has been developed in order to retrieve the true surface temperature of the PFC by solving low emissivity and additional parasitic flux coming from the reflections. This method relies on the comparison and the differences minimization between the experimental IR image and a synthetic IR image (obtained through a direct model).

The paper presents the inverse radiation method developed and applied to the WEST tokamak [2]. Section 2 focuses on the surface temperature error in WEST assessed from complete IR synthetic diagnostics. Section 3 describes the radiosity model used as a direct model in the inverse processing. Section 4 is dedicated to the inverse method. Finally, the paper deals with the results of this method to a numerical prototype of the WEST tokamak.

2. WEST tokamak

2.1 IR measurement in WEST

The WEST device is equipped with 12 IR cameras looking at the First Wall (FW), the heating antennas and the divertor, the most critical component receiving heat flux up to 20 MW/m².

IR synthetic diagnostic has been used to quantify accurately, for each camera, the impact on the surface temperature measurement of inaccurate emissivity, the reflections and camera resolution [3]. The synthetic diagnostic is based on a Monte Carlo ray-tracing (MCRT) code able to propagate rays in 3D geometry taking into account complex thermo-radiative properties of materials and inhomogeneous 3D temperature fields as inputs. Geometrical camera parameters (focal length, detector size) are used to reproduce the 2D IR image and the collected radiance by each pixel. The reflected light behavior is modeled through the Bidirectional Reflectivity Distribution Function (BRDF) and described as a combination of Lambertian and specular components. In first estimations, two extremes BRDF are considered: a diffuse model (100% Lambertian) and a highly specular model (2% Lambertian) following a Gaussian shape with a full-width half maximum of 12°.

In [4], it is showed that considering the target as blackbody (i.e. assuming that $\varepsilon=1$ instead of 0.2) induces an underestimation of the true target temperature up to 50% which is a risk for the machine safety. The contribution of reflected flux is assessed superior to 90% on colder targets (temperatures lower than150°C, the maximum temperature is around 1300°C), which causes an overestimation of temperature greater than 100%. This will affect especially the measurement of the profile decay length. The spatial resolution of the camera also affects the temperature measurement and may cause an error of 20% on the maximum temperature.

2.2 Numerical prototype tokamak-like

To test the inversion method, a numerical prototype tokamak-like with the main in-vessel components has

Author's email: charly.talatizi@cea.fr

been developed as illustrated in Fig. 1. The camera view looking at the lower divertor is reproduced (25°x58° field-of-view) since the lower divertor temperature measurement is the most critical.

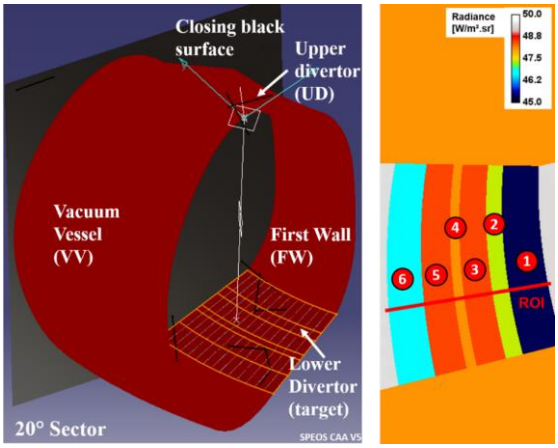

Fig. 1. Numerical tokamak-like prototype of WEST with the main PFC: the lower divertor, the Upper Divertor , the FW and the Vacuum Vessel (Left). Modeled radiance image obtained through the radiosity method in a baking scene (Right)

The input thermal scene of the tokamak is described on meshed geometries: each patch of the meshes is characterized by fixed temperature and emissivity values. Patches size requires to be optimized for each geometry to accurately describe the spatial distribution of temperature while limiting the number of patches to be solved in the equations describe in section 3. For instance, finer mesh is used for the lower divertor (about 160,000 patches of 12 mm mean size) characterized by a peaked temperature distribution, whereas coarse meshes (about 54,000 patches of 40 mm mean size) are used for the rest of geometry. Furthermore, in order to reduce again the patches number the tokamak model has been reduced to a 20° sector closed by two black surfaces at the environment temperature ($\varepsilon=1$). For an isothermal lower divertor (at 180°C) in an isothermal enclosure (at 200°C), the MCRT code shows an error of around 5% on the radiance collected by the camera detector between the whole tokamak (360°) and the 20° sector. This error can be reduced by increasing the closing surfaces temperature to compensate the missing flux due to multiple reflections outside the sector. In this study, the whole scene consists in about N=12,000 patches.

First experimental results [5] in WEST have shown that the emissivity on the lower divertor is not homogeneous because of the plasma-materials interaction (erosion/deposition phenomenon), see Fig. 2. In the numerical prototype, the emissivity profile along the components corresponding to the red line is then modeled as a piecewise constant profile with six values.

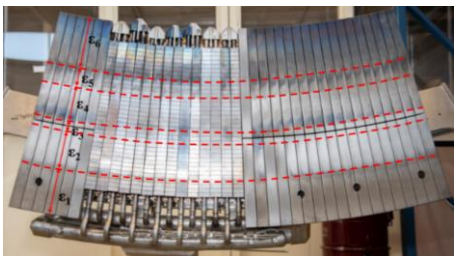

Fig. 2. Photography of the lower divertor sector and illustration of the piecewise constant profile constituted of six emissivities ($\varepsilon_1=0.2$, $\varepsilon_2=0.07$, $\varepsilon_3=0.1$, $\varepsilon_4=0.07$, $\varepsilon_5=0.15$ and $\varepsilon_6=0.3$ [5])

3. Radiosity model

The inversion method is based on an iterative processing aiming to minimize the differences between the modeled and the experimental IR images. The challenge is then to use a fast direct model able to simulate IR images for different input parameters (emissivity, BRDF, temperature) to compare them to experimental data.
The MCRT is not a direct model adapted to an iteration loop (not fast enough). This paper presents a faster direct model working in two steps: i) calculation of the view independent 3D solution (radiance of each patch) based on the radiosity method and ii) calculation of the desired 2D projection IR image. In the radiosity method, all the patches of the enclosure are assumed diffuse in emission and reflection (no specular reflection) [6]-[8].Then, the only radiative parameter needed for patch i is the emissivity ε_i ($i=1$ *to* N), because reflectivity is then given by $\rho_i = 1 - \varepsilon_i$. All the radiative quantities (emissivities and fluxes) are considered in the spectral range of the IR camera ($\Delta\lambda$=3.7 µm – 4.5 µm). The radiosity solution needs first the calculation of the N^2 diffuse view factors of the enclosure. For a given enclosure with a given meshing, this calculation is needed only once because the view factor between patches A_1 and A_2 is a purely geometrical quantity:

$$F_{A_1 \to A_2} = \frac{1}{A_1}\int_{A_1}\int_{A_2} \upsilon_{12}\frac{\cos\theta_1 \cos\theta_2}{\pi r_{12}^2} dA_2 dA_1 \qquad (1)$$

It represents the fraction (between 0 and 1) of radiation that leaves the surface A_1 and hits the surface A_2, where υ_{12} is an obstruction factor that takes the value 1 or 0 depending on whether surface dA_1 sees directly dA_2 or not [6].

The radiosity J for an opaque material is the amount of energy (emitted and reflected) leaving a surface in all directions, per unit area. The radiosity J_i of an elementary surface noted i is given by:

$$J_i = M_i + J_{r_i} = \varepsilon_i M^0{}_i + (1-\varepsilon_i)E_i \qquad (2)$$

Where M_i is the emitted component (exitance), ε_i is the emissivity; J_{ri} is the reflected component (reflectance). The exitance $M_i°$ is given by the spectral integration on $\Delta\lambda$ of Black Body Planck function at the temperature T_i [6]-[9]. The incident power E_i (irradiance) is the sum of radiation from all other surfaces that can hit surface i:

$$E_i = \sum_j F_{ij} J_j \qquad (3)$$

The equations *(2)* and *(3)* form a set of N linear equations with N unknowns J_i given by *(4)* or *(5)* in matrix form:

$$AJ = (I - RF)J = M \quad (4)$$

$$\begin{bmatrix} 1-\rho_1 F_{11} & -\rho_1 F_{12} & \cdots & -\rho_1 F_{1N} \\ -\rho_2 F_{21} & 1-\rho_2 F_{22} & \cdots & -\rho_2 F_{2N} \\ \vdots & \vdots & \ddots & \vdots \\ -\rho_N F_{N1} & -\rho_N F_{N2} & \cdots & 1-\rho_N F_{NN} \end{bmatrix} \begin{bmatrix} J_1 \\ J_2 \\ \vdots \\ J_N \end{bmatrix} = \begin{bmatrix} M_1 \\ M_2 \\ \vdots \\ M_N \end{bmatrix} \quad (5)$$

With, $I = (\delta_{ij})$ is the identity matrix, $R = (\delta_{ij}\rho_i)$ the reflectivity matrix, $F = (F_{Ai \to Aj})$ the view factors matrix and $M = (\varepsilon_i M^0{}_i(T_i))$ the emittance vector which is then called the "source term".

For N elementary surfaces in the 3D scene the view factors matrix is a $[N \times N]$ array. The view factors are computed with an integral contour calculation since there are no obstructions ($v_{12} = 0$) [10]. This matrix has a high computation time (72 million view factors for 12,000 patches, 12h computation time) but it can be obtained through parallel computing. When all J_i are computed through the resolution of (5), the radiance L_i (in W/m².sr) are deduced by $L_i = J_i/\pi$ (and $L_i°(T_i) = M_i°(T_i)/\pi$). Finally, the 3D to 2D projection of radiance L_i is achieved by an OpenGL routine to provide the observable quantity: the radiance collected by each pixel of the modeled pinhole camera or, in other words, the 2D IR modeled image (see an example on Fig. 1 (right)).

4. Inversion method

4.1 Methodology

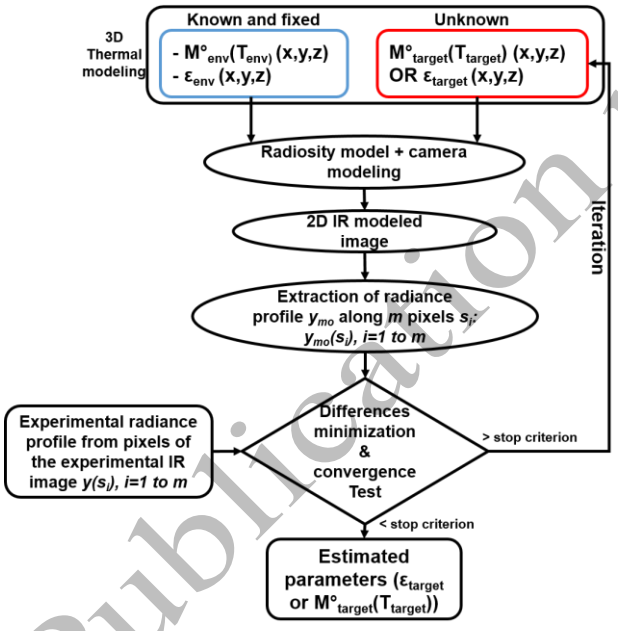

Fig. 3. Illustration of the parameters estimation problem

Fig. 3 illustrates the inversion process applied to IR measurements. From a set of input parameters, a 2D IR image is computed through the radiosity method coupled to the camera modeling. The parameters used as input of the direct model are related to the monitored thermal scene: the temperature and emissivity of the environment are assumed known while the temperature or emissivity of the target (lower divertor) are the p parameters x_j $(j=1 \text{ to } p)$ to be estimated. The Ordinary Least Squares (OLS) minimization between the experimental $y(s_i)$ and modeled $y_{mo}(s_i)$ data will be done on a radiance profile along m=230 pixels s_i $(i=1 \text{ to } m)$ corresponding to a radial line on the lower divertor (see the red line Fig. 1 (right)) and not all pixels of the image. The iterative minimization is stopped when variation of each parameter is inferior to 0.01% of its preceding value. The 95% confidence levels are then computed.

At each iteration of the OLS minimization, parameters are updated using Gauss-Newton algorithm [11]-[12]. That needs to invert the S^TS information matrix $[p \times p]$:

$$\boldsymbol{x}^{(k+1)} = \boldsymbol{x}^{(k)} + \left(\boldsymbol{S}^T\boldsymbol{S}\right)^{-1}\boldsymbol{S}^T\left(\boldsymbol{y} - \boldsymbol{y}_{\boldsymbol{mo}}(\boldsymbol{x})\right) \quad (6)$$

This algorithm is easy to implement and allows a minimum number of the direct model calls. Each column j of the sensitivity (or Jacobian) matrix S $[m \times p]$ contains the sensitivity coefficient of the model to the parameter x_j $(j=1 \text{ to } p)$ computed along pixels s_i $(i=1 \text{ to } m)$ given by equation (7) [11]-[12]:

$$S_j(s_i, \boldsymbol{x}) = \left.\frac{\partial \boldsymbol{y}_{\boldsymbol{mo}}(s_i, \boldsymbol{x})}{\partial x_j}\right|_{x_k \text{ for } k \neq j}, \quad j = 1 \text{ to } p,\ i = 1 \text{ to } m \quad (7)$$

The p parameters of the model are either the emissivities or the exitance M^0 of the patches of the 3D scene. The sensitivities to exitance are computed through the derivation of equation (4) with respect to exitance $M^0{}_j$:

$$\frac{\partial A}{\partial M^0{}_j} J + A\frac{\partial J}{\partial M^0{}_j} = \frac{\partial(\varepsilon M^0)}{\partial M^0{}_j} \quad (8)$$

The equation (8) can be reduced to equation (9) since the matrix A does not depend on the exitance $M^0{}_j$ of the patches in the 3D scene. In addition, the second term (the source term) is 0 everywhere except for the groups of patches that share the same $M^0{}_j$ value for which the source term is equal to their emissivity. These groups of patches (labeled k, m, n) do not necessarily have the same emissivity:

$$\Rightarrow A\frac{\partial J}{\partial M^0{}_j} = \left[[0]\ [\varepsilon_k]\ [\varepsilon_m]\ [\cdots]\ [0]\ [\varepsilon_n]\ [0]\right]^T \quad (9)$$

This equation shows that the sensitivity S_j to the exitance $M^0{}_j$ will be the solution of equation (9) that is the same as equation (4) with a specific source term. Equation (10) gives the sensitivity to the emissivity by derivating equation (4) with respect to ε_j:

$$-\frac{\partial(RF)}{\partial \varepsilon_j} J + A\frac{\partial J}{\partial \varepsilon_j} = \left[[0]\ [0]\ \left[M^0{}_r\right]\ [\cdots]\ [0]\ \left[M^0{}_s\right]\ \left[M^0{}_t\right]\right]^T \quad (10)$$

In this case, the matrix A and more particularly the matrix product (RF) depends on ε_j. The second term (the source term) is 0 everywhere except for the groups of patches that share the same ε_j for which the source term is equal to the difference between their exitance M^0 and their irradiance E (given by FJ). These groups of patches (labeled r, s, t) do not necessarily have the same $(M^0\text{-}E)$ value:

$$A\frac{\partial J}{\partial \varepsilon_j} = \left[[0]\ [0]\ \left[M^0{}_r - E_r\right]\ [\cdots]\ [0]\ \left[M^0{}_s - E_s\right]\ \left[M^0{}_t - E_t\right]\right]^T \quad (11)$$

Then the inverse of matrix A already computed to solve (8) is advantageously reused to solve the sensitivity equations (9) and (11). This is the same idea developed in [13] but with Monte-Carlo algorithm instead of radiosity algorithm.

It is worth plotting the reduced sensitivity $x_j S_j(s_i)$ for different parameters of models along a pixel line (Region Of Interest, ROI) on the lower divertor. The reduced sensitivities are used to compare directly the parameters

between them and then figure out the most influent parameters and where this influence occurs. This comparison is also used to detect if some sensitivities are similar which would be bad for the conditioning of the information matrix S^TS that has to be inverted.
Consider the situation illustrated in Fig. 2 where the lower divertor (LD) is assumed split in 6 annular strips of different radiative properties and temperatures but each strip has an homogeneous emissivity and is at an homogeneous temperature. The lower divertor is enclosed in the surrounding surfaces (Upper Divertor, UD, FW and Vacuum Vessel, VV) described in Fig. 1. Each of them has a homogeneous emissivity and a homogeneous temperature. This model then has 18 different parameters: 6 emissivities and 6 exitances for the lower divertor, 3 emissivities and 3 exitances for the surrounding surfaces. Fig. 4 shows the reduced sensitivities of the model to the emissivity and the exitance of strip #3 and to the emissivity of the UD, VV and FW (5 of the 18 parameters):

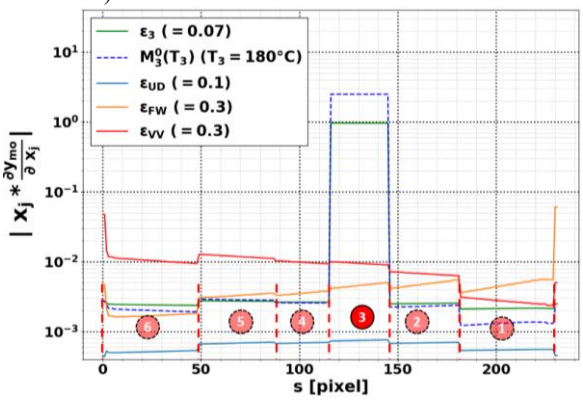

Fig. 4. Reduced sensitivities of model with respect to some parameters: emissivity and exitance of strip #3 of LD, emissivities of UD, FW and VV. The model output is the profile of collected radiance on m=230 pixels for an isothermal (180°C) lower divertor, the other 3 parts of tokamak (UD, FW, VV) being isothermal at 200°C, with their own emissivities

The sensitivity of the model to one of the emissivities of the target (here the #3) is almost zero everywhere except on the concerned strip. The observation is analog for the exitance. Furthermore, the sensitivities of the model to the emissivities of the environment are negligible and there is no need to include them in the Parameters Estimation Problem. At last, the sensitivity study illustrates also that the sensitivities to an emissivity and to an exitance of a same strip (here #3) are correlated; hence, it is not possible to estimate those two parameters simultaneously, which is a well-known issue; multispectral measurements are usually used to try to solve the emissivity and temperature correlation [14]-[15].

4.2 Application to WEST

Further to the emissivity and temperature correlation issue, two kinds of experimental thermal scenes (named "baking" and "heatload") are proposed to be used for estimating independently emissivity and temperature parameters. This is possible with WEST experiments since its operation plans baking for which the surface temperature of all in vessel components is uniform and measured punctually thanks to embedded diagnostics (thermocouples and Fiber Bragg Grating).
The inversion method to retrieve the true surface temperature of PFC will then occur in two steps: i) use of a baking scene, for which the surface temperatures are well known, to estimate the emissivity of the target and ii) use of the resulting emissivity map to estimate the surface temperature of the target during heatload scenes.

5. Results

5.1 Confidence and Precision of the Inverse Method

To test the inverse processing, synthetic measurements including an additive Gaussian white noise have been generated from the radiosity method. The standard deviation of this noise is σ=0.155 W/m².sr (roughly estimated by considering photon noise and background noise). For the baking scene, this noise is roughly 4% of the range of magnitude of measured radiances. As for the heatload case, the noise is respectively 3% and 0.04% of the minimum and maximum measured radiances.. The covariance matrix resulting of the amplification of this noise is given by the following formula [11]-[12]:

$$Cov(x) = \sigma^2 (S^T S)^{-1} \qquad (12)$$

Where x is the vector of estimated parameters (ε or M^0) corresponding to the solution of the radiosity linear system and S the sensitivity matrix computed for x. The 95% confidence intervals of the estimated parameters are computed from this covariance matrix: $x \pm 1.96 \cdot diag(Cov(x))^{1/2}$.

5.2 Emissivity estimation

The emissivity estimation is performed from infrared measurements during the baking scenario. The temperatures of the target and environment are assumed known. The sensitivities to the emissivities of the surrounding surfaces are negligible then they will not be estimated but they are fixed to their value of the literature (0.1 for the UD made of tungsten, 0.3 for the FW and VV made of stainless steel). The simulated input thermal scene is the following: the temperature of the surrounding surfaces (i.e. UD, FW, VV and the black surfaces) is fixed to 200°C and the temperature of the divertor to 180°C. The divertor emissivity profile, that we try to solve, is the one described in section 2.2, composed of 6 strips with emissivity values varying between 0.07 and 0.2.
However, in the inverse processing, we do not impose the spatial variation of emissivity on these 6 strips as a priori knowledge.
The component is split into 40 regular annular strips of uniform emissivity. The inversion method will then consist in estimating the emissivity of the 40 strips and hopefully retrieve the "6 strips" profile. The number of strips is optimized to describe the emissivity profile in sufficient details while limiting the number of parameters to be estimated. In this case, the number of strips is constrained by the target mesh size (10 mm).
Fig. 5 (left) shows the optimal radiance profile in the camera plane (obtained with the optimal estimated emissivity values in the 'real world', Fig. 5 (right))

compared to the 'measured' radiance profile (synthesized with noise here).
It is worth noting that the method converges quickly (in 4 iterations) and this, without applying high constraint on the initial guess. As proof, the initial estimated radiance profile shown in Fig. 5 is the result of 40 emissivity initial values randomly fixed between 0 and 1.
The errors on the estimated radiance profile are up to 3%. The estimated and synthetic profile are in good agreement, the greater discrepancies occur at important transitions of the emissivity values. This results in high errors on the emissivity up to 40%. However the mean error on the emissivity values is much lower (6%).

5.3 Temperature estimation

The inversion method for solving the surface temperature from experimental data is equivalent to the one for solving the emissivity as described in 5.2. The temperature of the surrounding surfaces is assumed known (fixed to 90°C) and the emissivities of LD are known resulting of the first estimation step from IR images obtained during the baking.

The divertor temperature profile, that we try to solve, follows a profile given [16]. The exitances of the 40 different strips of LD (see section 3) are estimated with the method described in section 4.1.
The system converges quickly (in 2 iterations) for the exitance estimation because the Parameter Estimation Problem is here linear. From the resulting exitance, it is possible to retrieve the surface temperature of the strips since the exitance $M_i°(T_i)$, given by the spectral integration of Planck function at the temperature T_i, is monotonous. Fig. 6 (left) presents the comparison between the estimated temperatures and the true surface temperatures on the lower divertor. Fig. 6 (right) also shows the usual interpretations of IR measurements, pixel by pixel, to retrieve the temperature of the target. The apparent temperature is obtained through Planck's function inversion assuming $\varepsilon=1$ (blackbody assumption), whereas the pure emitter temperature uses the true emissivity assumed well known for each pixel of the profile but does not consider any reflection:

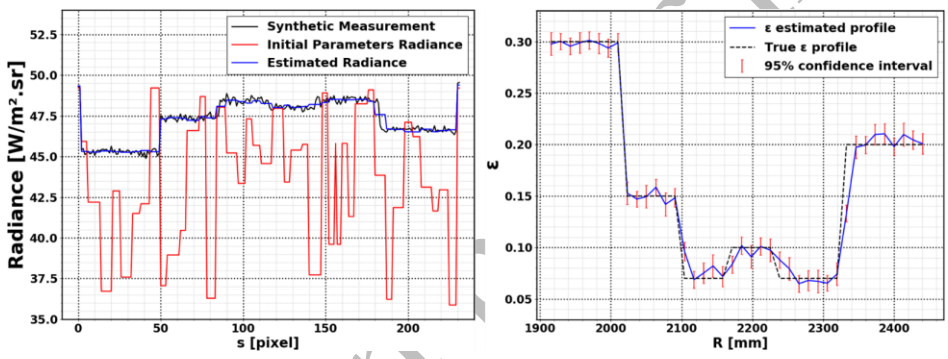

Fig. 5. Left: Optimal estimated radiance profile (red) obtained after the convergence of the inverse method compared to the 'measured' profile (black, synthesized with noise here) and to the initial estimated radiance profile (blue). Right: Optimal estimated emissivities (blue) in a baking scene compared to the true emissivities (dashed black). The estimated values are given with the 95% confidence intervals

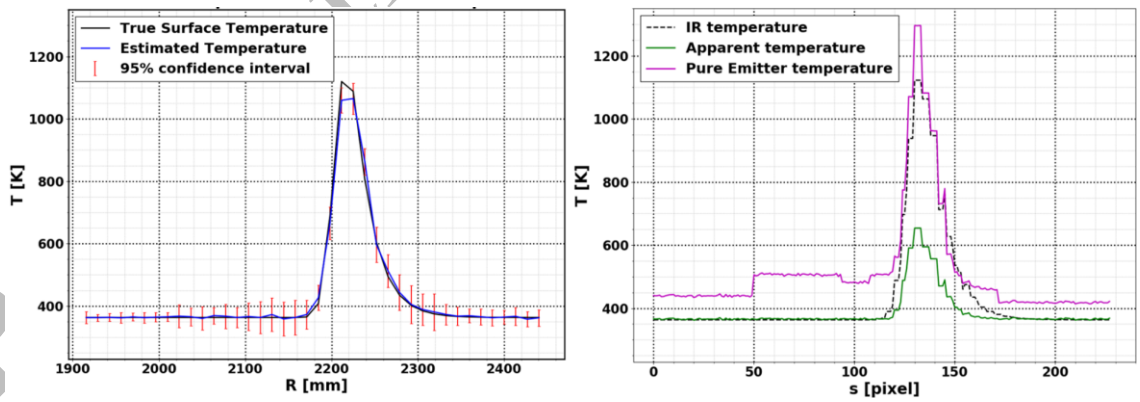

Fig. 6. Left: Estimated temperatures (blue) with associated confidence intervals during a plasma scenario compared to the true temperatures (black) – Right: Planck function inversion applied to the synthetic data results in a profile of apparent temperatures (blackbody assumption, ε=1) (magenta) or in a profile of pure emitter temperatures (emissivities assumed known per pixel) (green)

In the 'real world' (Fig. 6 left) there is 1% error on the maximum temperature profile and up to 3% error on the colder temperature (i.e. 90°C, the temperature of the environment) between estimated and true temperatures.
In the image world (with pixels, Fig. 6 right), the apparent and pure emitter temperatures are compared to the so-called IR temperature that corresponds to the true temperature profile in the real world after degradation by the 3D→2D projection and pixel sampling. The error on the peak between the true temperature and the IR temperature is negligible (inferior to 0.5%). Table 1 presents the two comparison, in 'image world' and in 'real world':

Table 1. Error on the surface 'IR temperature' measurement assuming a blackbody ($\varepsilon=1$, so-called BB T°), known emissivity without solving the reflections (so-called PE T° for 'Pure Emitter'). Error on the 'true surface temperature' measurement with the inverse method (so called estimated T°).

	In 'image world'		In 'real world'
	BB T° vs IR T°	PE T° vs IR T°	Estimated T° vs true T°
Peak	42%	15%	1%
Cold targets	6%	11%-40%	3%

6. Conclusion

The paper presents an inversion method to retrieve the surface temperature from IR measurements solving the reflections in an all-reflective environment. To do so, the baking scene, in which the uniform temperatures of the target and the environment are known, is first used to estimate the target emissivity profile with a mean error of 6%. The target surface temperature is then retrieved during a plasma scenario with an error better than 3% on the peak and on colder targets, the most disturbed by the reflections.

The inverse method based on radiosity model gives good results for all diffuse thermal scenes and knowing the environment temperature (which is a realistic assumption since the wall is actively cooled). The next step will consist in testing the accuracy of the method for retrieving the surface temperature in the case of highly specularly reflective surface. To achieve that the MCRT code will be used as a generator of synthetic measurements with materials presenting a highly specular BRDF model.

Furthermore, the method is currently not limited by the number of parameters but rather by the constraints put on the meshes precision for computing time issues. This can cause high errors on the emissivity estimation if the discretization cannot follow the radiative properties important transitions along the target. These errors can decrease with an optimization of the mesh size.

To go further the inversion processing will be tested on experimental data from WEST and ASDEX Upgrade.

Acknowledgements

This work has been carried out within the framework of the EUROfusion Consortium. The views and opinions expressed herein do not necessarily reflect those of the European Commission.

References

[1] Aumeunier M.-H. et al, 2017, *Nuclear Materials and Energy* 12, Pages 1265-1269.

[2] J. Bucalossi, et al., The WEST project: Testing ITER divertor high heat flux component technology in a steady state tokamak environment. *Fusion Eng. Des*. 89 (2014), 907–912.

[3] Aumeurnier M.-H. et al., 2012, IEEE Transactions on Plasma Science, 40, 3.

[4] Talatizi C. et al., Thermique et sciences de l'information, Tome1, Actes du Congrès annuel de la Société Française de Thermique, SFT 2018 (ISBN : 978-2-905267-95-5).

[5] Fedorczak N. et al., *Infra-red thermography estimate of deposited heat load dynamics on the lower tungsten divertor of WEST*, under review PFMC 2019.

[6] Siegel, R. and Howell, J.R. Thermal Radiation heat transfer, 4th edition, CRC Press 2001

[7] Dutre P., Bekaert P., Bala K., Advanced Global Illumination, 2nd Ed., A. K. Peters Ltd, 2006

[8] Sillion F., Puech C., Radiosity and Global Illumination, M. Kaufman Publishers Inc., 1994

[9] Michael F. Modest, Radiative Heat Transfer, 3rd Edition, Academic Press 2013

[10] Sara C. Francisco et al., 2014, Calculation of view factors for complex geometries using Stokes' theorem, Journal of Building Performance Simulation.

[11] Richard C. Aster, Brian Borchers, Clifford H. Thurber, Parameter Estimation and Inverse Problems, Academic Press, 2013.

[12] B. Rémy, S. André, Thermal Measurements and Inverse Techniques, Chapter 9 Nonlinear Estimation Problems, CRC Press 2011

[13] Caliot, C. et al., *Validation of a Monte Carlo Integral Formulation Applied to Solar Facility Simulations and Use of Sensitivities*, Journal of Solar Energy Engineering, 137(2), 021019.

[14] J. C. Krapez, Thermal Measurements and Inverse Techniques, Chapter 6 Radiative measurements of temperatures, CRC Press 2011

[15] Herve P. et al., Infrared technique for simultaneous determination of temperature and emissivity, 2012, Infrared Physics & Technology, 55, 1.

[16] T. Eich, et al., J. Nucl. Mater. 438 (2013) S72-S77.